ACS OMEGA

http://pubs.acs.org/journal/acsodf

Article

Hierarchical Lignin-Based Carbon Matrix and Carbon Dot Composite Electrodes for High-Performance Supercapacitors

Lu Yu, Chien-Te Hsieh,* David J. Keffer, Hao Chen, Gabriel A. Goenaga, Sheng Dai, Thomas A. Zawodzinski, and David P. Harper*

Cite This: *ACS Omega* 2021, 6, 7851−7861

Read Online

ACCESS | Metrics & More | Article Recommendations | Supporting Information

ABSTRACT: This work adopts an efficient chemical-wet method to build a three-dimensional (3D) carbon composite as an electrode material for high-performance supercapacitors (SCs). Carbon dots (CDs), prepared by thermal pyrolysis of citric acid and urea under microwaves at 280 °C, are homogeneously coated onto lignin-based activated carbons (ACs), thus forming the 3D composites possessing an interior surface decorated with CD binding sites. Benefiting from the hydrophilicity and ultrafine size of CDs, the affinity of the electrode surface toward aqueous electrolytes is significantly improved with the addition of CDs, leading to the enhanced effective surface area (i.e., abundant electroactive sites) and a decreased ionic diffusion path. The capacitance of the SCs is improved from 125.8 to 301.7 F g^{-1} with CD addition. The SC with CD addition possesses improved cycle stability with a coulombic efficiency around 100% after 3000 cycles. After cycling, the ion diffusion coefficient of the CD@AC-11 electrode is enhanced by 25.5 times as compared to that of the pristine AC one. This unique and robust carbon framework can be utilized for engineering the desired pore structure and micropore/mesopore fraction within the AC electrodes. This strategy of CD@AC electrodes demonstrates a promising route for using renewable porous carbon materials in advanced energy-storage devices.

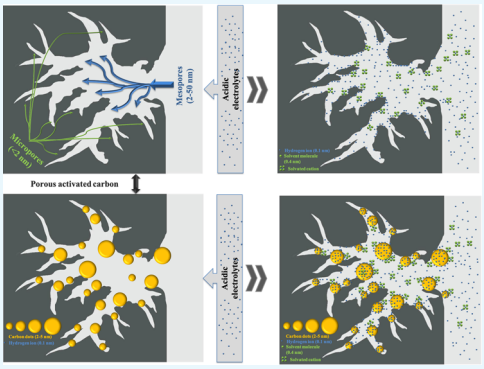

1. INTRODUCTION

With the increasing need for energy storage and environmental substantiality, supercapacitors (SCs) promise to be important energy-storage devices possessing a high power density, a long cycle life, excellent cycling stability, and a low cost.[1−3] Based on different work mechanisms, SCs are generally classified into faradaic pseudo-capacitors and electric double-layer capacitors (EDLCs).[4,5] Theoretically, pseudo-capacitance originates from the faradaic process between the electrodes and electrolytes *via* charge transfer across the interface. Transition-metal oxides and conductive polymers, which possess redox sites and intrinsic high electrical conductivity, are typical pseudo-capacitive materials.[6,7] EDLCs are based on the Helmholtz model that the charges are separated at the polarization interface between the electrode and electrolyte. There is no charge transfer involved in favor of reversible adsorption and desorption. This energy-storage mechanism enables a quick charge/discharge rate as well as superior cyclability.[8−10] Versatile activated carbon (AC) materials have been extensively studied as electrodes for EDLCs as they possess the high specific surface areas (SSAs) needed for high capacity.[11,12] However, it is generally recognized that not all pores are electrochemically accessible; imperfect connectivity of the porous network leaves some pore volume inaccessible to ions.[13] In addition, tortuous microporosity leads to long diffusion distances, thus resulting in relatively high ionic diffusion resistance.[14] Pioneering work has been devoted to maximizing the accessible SSAs of ACs, such as heteroatom doping into the porous carbon framework to increase the wettability,[15−17] modifying pore distribution by using different precursors,[18] and matching electrolytes.[19−21]

Lignin is an organic polymer with a condensed carbon backbone structure and complex aromatic functional linkages.[22] After pyrolysis and activation, there is still a small amount of impurities, such as N and O, which provide extra electroactive sites.[23,24] However, the porous structure of lignin-based ACs consists predominantly of narrow micropores,[24−26] a significant fraction of which remains inaccessible to ions. This drawback greatly limits effective surface areas, porous accessibility, and wettability of lignin-based carbon electrodes.

Carbon dots (CDs), also called "carbon quantum dots", are highly crystallized zero-dimensional materials which have been used in various energy applications due to their excellent

Received: January 25, 2021
Accepted: February 26, 2021
Published: March 10, 2021

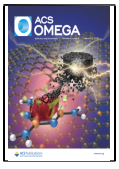

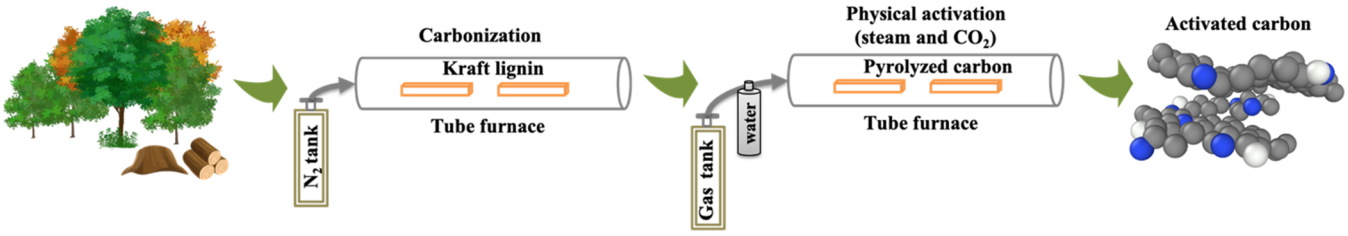

Figure 1. Preparation routine of ACs *via* carbonization of Kraft lignin and two-step physical activation using steam and carbon dioxide as activation agents.

electrochemical properties and ultrafine particle size.[27−30] CDs usually have a very small particle size, ranging from 2 to 30 nm. Abundant functional groups, such as carboxylic, carbonyl, and amino groups, tend to bond with the carbon core or on the CD surface. The presence of surface functionalities leads to high hydrophilicity of CDs and homogeneous dispersion in polar solvents.[30,31] The high functionality suggests the use of CDs as active sites, decorating the interior pore space of ACs, where they can interact with ions or hydrating species during the charge/discharge process. Researchers have tried to integrate CDs into the porous carbon frameworks by the one-step calcination-activation method and employed them as the EDLC materials. With the CDs fused into the carbon skeleton, the surface roughness was increased, thus achieving a high surface area, which led to the higher capacity.[32,33] CDs were also applied as the electrodes for batteries and achieved better cycle ability and higher capacity due to the special carbon frame structure with a larger interlayer space and a large surface area.[34]

In this work, we applied N-doped CDs and mixed with lignin-based ACs under an optimized ratio, making the CDs fully and uniformly distributed on the surface of the highly porous AC matrix to form a three-dimensional (3D) carbon composite with an interior surface decorated with CDs. Instead of optimizing the inner porous structure, countless hydrophilic binding sites are created by CDs on the stable AC matrix to provide abundant electroactive sites with excellent cyclability. In the novel design of carbon composites, superhydrophilic CD sites are more attractive to ionic species and solvated electrolyte ions in aqueous media, compared with the undecorated deep and branched micropores. Meanwhile, with CDs evenly attached to the surface of ACs, more aqueous electrolytes can migrate and diffuse into the porous network, thus increasing contact with the electrodes. Accordingly, the CDs significantly shorten the ionic diffusion path, which leads to an efficient ionic diffusion and a decreased mass-transfer resistance. This research proposes a simple design to achieve high-performance SCs with a facile fabrication method. With the verification of characteristic measurements, we proved the effectiveness of this method and the feasibility of the 3D carbon composite, which could also be applied in a variety of energy-storage devices, such as carbon electrodes for EDLCs and ion-storage batteries and catalyst electrodes for fuel cell and photovoltaic cells.

2. EXPERIMENTAL SECTION

2.1. Preparation of ACs and CDs. The AC sample was made from commercial Kraft lignin. It was carbonized in a ceramic boat inserted in the alumina tube furnace with nitrogen flow at 700 °C for 1 h. After naturally cooling down with N_2 flow, the samples were pulverized by hand, grinding into small pieces, followed by ball milling (PM100 RETSCH model), where the mill contained 2 and 10 mm stainless-steel balls in a stainless-steel container at 350 revolutions per minute for 45 min. After that, the ground carbon powders were separated using sieves from grinding balls and placed into the tube furnace for steam activation at 800 °C for 0.5 h with a ramping rate of 10 °C min^{-1}. After steam activation, the sample was exposed to a CO_2 atmosphere for continuous physical activation at 800 °C for 1 h to produce the final AC samples (shown in Figure 1).

The CDs are prepared by a solid-phase microwave-assisted method, heating the mixture of citric acid and urea at 280 °C for 5 min according to our previous study.[28]

2.2. Materials Characterization. The morphology and microstructure were observed by high-resolution transmission electron microscopy (HR-TEM) (ZEISS, LIBRA 200) and scanning electron microscopy (SEM) (Phenom ProX). The crystal structure of ACs and CD samples was characterized by X-ray diffraction (XRD) (Empyrean, Panalytical). The surface functional groups on the carbon composites were inspected and collected with a Fourier transform infrared (FTIR) spectrometer (PerkinElmer, Llantrisant). The chemical compositions of samples were characterized by X-ray photoelectron spectroscopy (XPS, Fison VG ESCA210). The contact angle was measured using a Krüss FM40 shape analysis system (Hamburg, Germany). A 2 μL water droplet was deposited on the substrate, and the static time was 5 s. N_2 adsorption and desorption isotherms were obtained using a TriStar 3000 volumetric adsorption analyzer (Micromeritics Instrument Corp.). SSAs and mesopore volumes were determined from Brunauer−Emmett−Teller (BET) and Barrett−Joyner−Halenda equations, respectively. The pore size distribution of the carbon samples was derived from density function theory (DFT) calculation.

2.3. Electrochemical Performance Evaluation. Electrochemical measurements of the ACs and CD electrodes were taken using a three-electrode configuration system with 2 M H_2SO_4 as the electrolyte solution. Pt wire served as the counter electrode, and Ag/AgCl served as the reference electrode. The ACs and CDs are uniformly mixed with Nafion and deionized water and then dropped and coated on a carbon paper with an area of 2 × 1 cm^2. The stainless-steel foil was applied as the current collector. The cyclic voltammetry (CV) measurements of the electrodes were performed within the potential range between 0 and 1.0 V versus Ag/AgCl, and the scan rates were set at 10, 30, 50, and 100 mV s^{-1}. The capacitances were measured by galvanostatic charge−discharge (GCD) measurements within the voltage region of 0−1.0 V. The impedance spectra were recorded with the frequency ranging from 100 kHz to 10 mHz. *Z*-view software simulated the impedance behavior based on Nyquist plot data.

https://dx.doi.org/10.1021/acsomega.1c00448
ACS Omega 2021, 6, 7851−7861

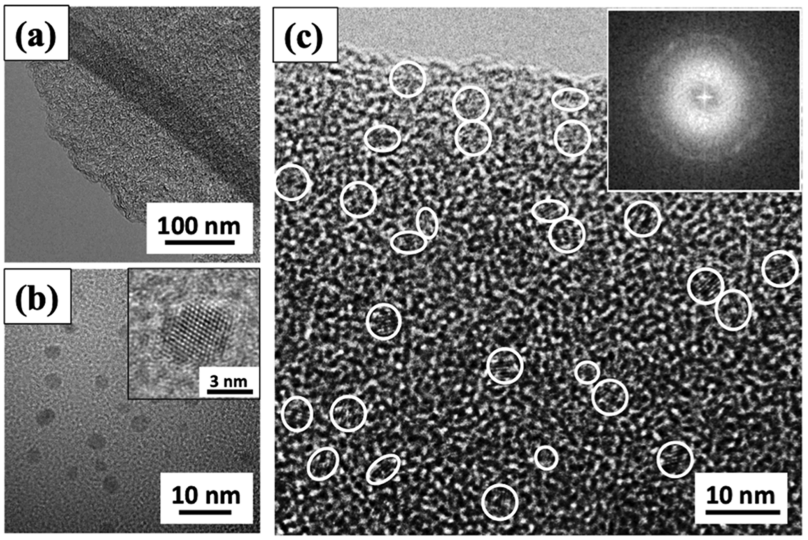

Figure 2. HR-TEM micrographs of (a) ACs, (b) CDs, and (c) CD@AC-11 samples. The insets of (b,c) show well-ordered lattice fringes of a diffraction pattern of an individual CD within the selected area.

3. RESULTS AND DISCUSSION

For clarification, the electrodes fabricated with mixed CDs and ACs at mass ratios of 1:1 and 1:2 are designated as CD@AC-11 and CD@AC-12, respectively. The HR-TEM micrograph of the prepared ACs is shown in Figure 2a, which exhibits an amorphous morphology with disordered carbon layers. The obtained CDs with a uniform size distribution of 2−5 nm are shown in Figure 2b. Clearly, the crystal lattice of a CD can be observed in the inset of Figure 2b. After the CDs are deposited on the surface of the ACs, CD domains with the crystalline structure evenly distribute on the AC matrix in Figure 2c. The selected-area electron diffraction pattern, as shown in the inset of Figure 2c, indicates the presence of bright diffraction rings and spots and suggests that the CDs consisted of nanocrystallites.

The SEM images of as-prepared electrodes with AC and CD@AC-11 on the carbon paper are shown in Figure 3. We observe that the carbon paper is composed of a number of microscaled fibers with a random orientation. ACs fully covered the surface of the fibers, indicating that Nafion is an effective adhesion agent. As for the CD@AC-11 electrode, it is obvious that CDs are uniformly attached to the ACs, resulting in a high coverage of CDs on the fibers.

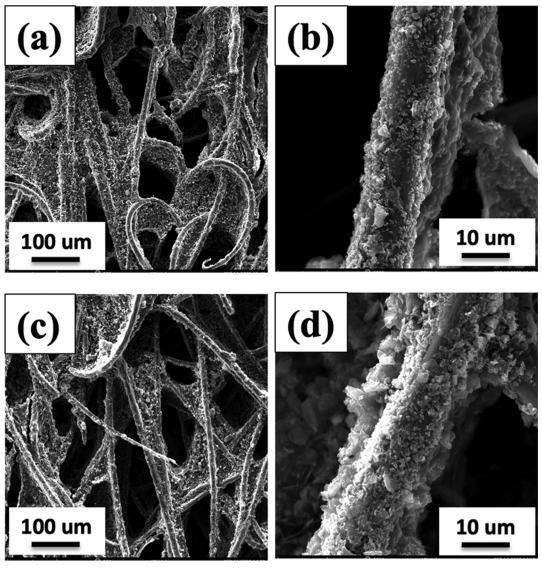

Figure 3. SEM images of (a,b) AC and (c,d) CD@AC-11 carbon paper electrodes with low and high magnification.

The XRD pattern of AC, as illustrated in Figure 4a, shows a broad lump located at ∼24°, corresponding to the characteristic (002) diffraction peak of carbons. The dispersive and broad peak indicates the amorphous structure of carbon with a large interlayer spacing distance ($d_{(002)}$ = 0.370 nm). The (002) peak of CD located at ∼27° shows much sharper, implying the presence of a well-crystallized structure. The intensity of the peak in the CD@AC-11 sample is higher than that of AC, which indicates higher crystallinity than amorphous AC. Interestingly, the small twin peak could be observed in the enlarged image, commonly ascribed to the interlayer stacking reflections.[28,35] The peak location shifts right, compared to the AC peak, indicating that the interlayer spacing distance decreases from 0.370 to 0.330 nm due to the coverage of CDs on the surface of ACs. The small sharp peak (2θ: ∼30°) in AC and the CD@AC-11 sample originates from the presence of iron oxide coming from the ball milling of the carbonized lignin.[36,37]

Figure 4b illustrates the FTIR spectra of AC, CD, and CD@AC-11. In the CD spectrum, the valley at 1580 cm^{-1} corresponds to the C−C stretching in the transmission spectrum, whereas C−O groups appear at 1142 and 1047 cm^{-1}. The bands at 3450 cm^{-1} and 1720 cm^{-1} correspond to hydroxyl (−OH) and carbonyl (C═O) groups, respectively. Strong bands at 1357 and 3200 cm^{-1} provide evidence of C−N groups, confirming N-functionalized CDs.[23,38−40] It is worth noting that CD@AC-11 shows a similar spectrum with CD, indicating that functional CDs are uniformly covered on the AC surface. Besides the enhanced absorption from C═O and C−O groups, it is apparent that abundant C−N groups are introduced since the CDs possess a high amidation level due to N-dopants and N-functionalities. This is further confirmed by the XPS measurement, which is shown in Figure 5a. The presence of the N 1s peak in the CD@AC-11 sample proves that the introduction of CDs leads to more C−N functional

https://dx.doi.org/10.1021/acsomega.1c00448
ACS Omega 2021, 6, 7851−7861

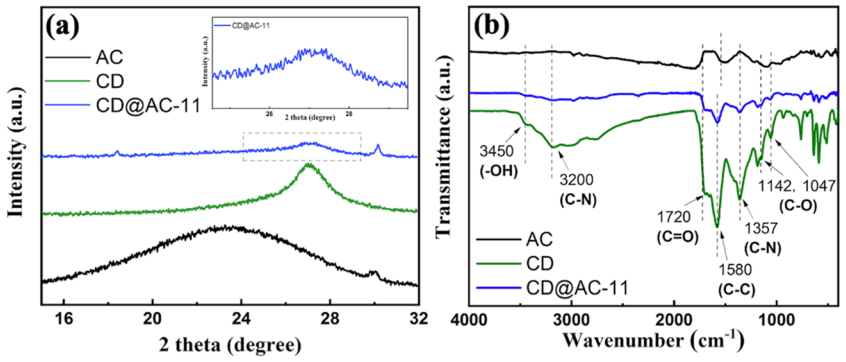

Figure 4. (a) XRD patterns and (b) FTIR spectra of AC, CD, and CD@AC-11 samples.

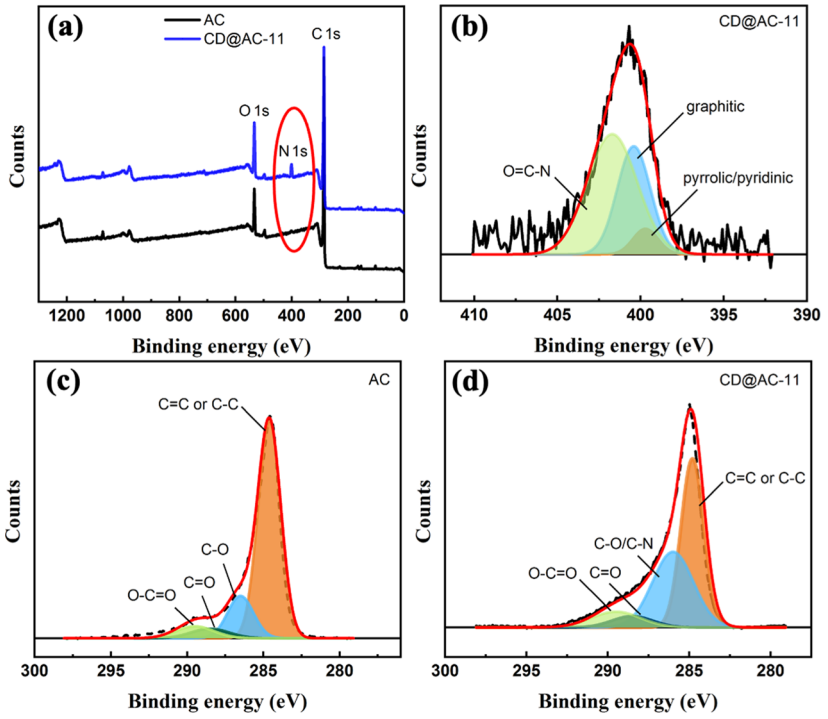

Figure 5. (a) Survey-scan XPS spectra of AC and CD@AC-11 samples; (b) N 1s peak of the AC@AC-11 sample and the C 1s peak deconvoluted by a multiple Gaussian function; (c) AC and (d) CD@AC-11 samples.

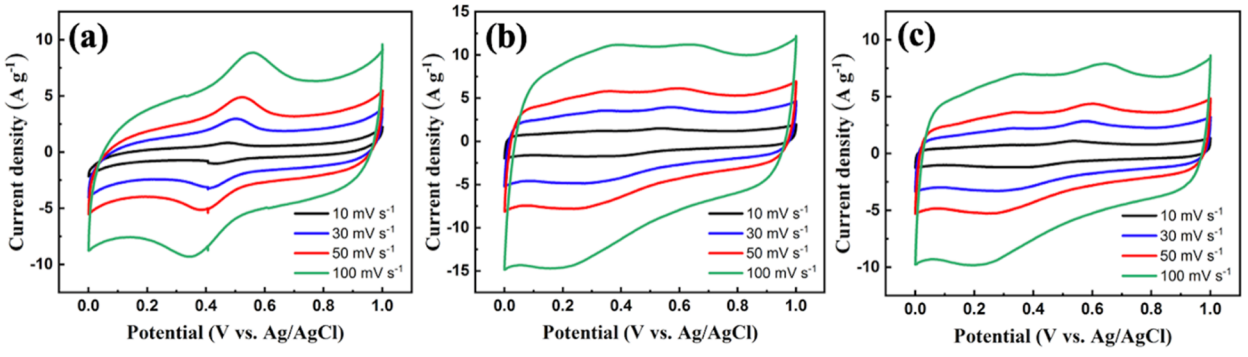

Figure 6. CV curves of (a) AC, (b) CD@AC-11, and (c) CD@AC-12 electrodes at different scan rates.

groups. The high-resolution XPS spectra of the N 1s peak of CD@AC-11 are shown in Figure 5b. The N 1s peak was deconvoluted into three peaks centered at 399.7 eV (pyrrolic/pyridinic N), 400.4 eV (graphitic N), and 401.7 eV (O═C−N).[28,41] Usually, the first component represents the aromatic C═N−C, the graphitic N refers to the N bonded with three sp^2 carbon atoms, and the last one is the amino group.[28] In our case, the graphitic and amino N are predominant since they take 31.9 and 56.4% of the total integration area, respectively. The C 1s spectra of AC (Figure 5c) were decomposed into four peaks and represent C═C or C−C (*ca.* 284.6 eV), C−O (*ca.* 286.5 eV), C═O (*ca.* 288.5 eV), and O−C═O (*ca.* 289.5

https://dx.doi.org/10.1021/acsomega.1c00448
ACS Omega 2021, 6, 7851−7861

eV).[19] This can be attributed to the existence of oxide functional groups attached to the edge and surface of ACs as well as the CDs. While for CD@AC-11, one more peak centered at 285.2 eV refers to the presence of C−N (Figure 5d).[14,16] To further verify the result, we also conducted the CHNS-type elemental analysis. The N/C ratio of the CD@AC-11 sample is increased up to 16.1%, much higher than that of AC (i.e., 3.8%). This enhanced N/C ratio is attributed to the fact that CDs contain a high N/C ratio (*ca.* 45.6%). Accordingly, this result agrees with FTIR and XPS analysis, revealing that more N-containing functional groups are introduced onto the surface of the porous structure of ACs.

The electrochemical measurements were conducted using a three-electrode system in a 2 M H_2SO_4 aqueous electrolyte to verify the performance of the as-fabricated electrodes. Figure 6 shows typical CV curves of SCs fabricated with AC, CD@AC-11, and CD@AC-12. It is obvious that the CV curves of the pristine AC electrode (see Figure 6a) show a pair of redox peaks, possibly originating from faradaic reactions occurring on the electric double layer due to heteroatoms (N, H, and O) derived from precursors and trace iron oxide in the lignin-based AC.[9,10] The CV profiles of CD@AC-11, as shown in Figure 6b, exhibit near rectangular shapes that contain multiple redox peaks, indicating the coexistence of two different energy-storage mechanisms, that is, electric double-layer formation and faradaic redox reaction.[41] The relatively rectangular shape of the curves and the increased area stem from the electric double-layer behavior. The introduction of various functional groups leads to the obviously increased amount of hydrophilic polar sites, significantly enhancing the affinity toward the aqueous electrolyte and providing more accessible surface area to ions. In the ideal formation of the carbon electric double layer with the acid electrolyte, the charge and discharge process of carbon electrodes could be expressed as eq R1[42,43]

$$C^* + H^+ \leftrightarrow C^*//H^+ \quad \text{(R1)}$$

where the carbon electrode is represented as C*, the proton of the acidic electrolyte is represented as H^+, and $C^*//H^+$ represents the double layer where charges accumulated separately on the two // sides. It is simply the physical adsorption process forced by the electrostatic forces between carbons and protons. In our case, besides porous carbons, abundant surface oxygen and nitrogen functional groups provide more available adsorption and desorption sites. The equilibrium reactions which occurred are presented as eqs R2 and RR3[6,11,42,44]

$$C_xO^* + H^+ \leftrightarrow C_xO^*//H^+ \quad \text{(R2)}$$

$$C_xN^* + H^+ \leftrightarrow C_xN^*//H^+ \quad \text{(R3)}$$

where C_xO^* and C_xN^* represent oxygen-containing (e.g., carbonyl and quinone groups) and nitrogen-containing functional groups (e.g., amino, quaternary, and pyrrolic/pyridinic N groups), respectively. Herein, $C_xO^*//H^+$ and $C_xN^*//H^+$ represent the electric double layers with charges accumulated on the sides due to the ion−dipole attraction, which is different with electrostatic forces between carbons and protons. The increased electric double-layer behaviors are partially derived from the enhanced dipole−dipole interactions.

For confirmation, we conducted contact angles measurements to directly examine the hydrophilicity of the electrodes. As shown in Figure 7, the results confirm our speculation that

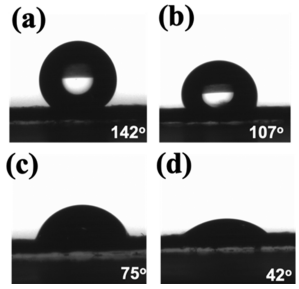

Figure 7. Optical microscopy images of water droplets on (a) carbon paper, (b) AC electrode, (c) CD@AC-11 electrode, and (d) CD electrode.

the CD electrode shows super hydrophilic behavior with the contact angle of 42°. With the help of CD decoration, the contact angle exhibits an obvious decrease from 107 to 75°, which clearly demonstrates that the addition of CDs greatly improves the hydrophilicity of the electrodes and thus enhances the surface affinity toward the aqueous electrolyte. This result further proves the feasibility of eqs R2 and RR3.

The presence of nitrogen and oxygen functional groups contributes improvement to the electric double-layer capacitance and the pseudo-capacitance, as evidenced by the redox peaks. We hypothesize that the N functional groups significantly improve the electrochemical reactivity due to their electron-donor properties. Specifically, negatively charged pyridinic/pyrrolic N atoms provide electroactive sites and facilitate the possible redox reactions. The simplified reaction equation is expressed as eq R4[10,14,44−46]

$$C_xN^* + H^+ + e^- \leftrightarrow C_xNH^- \quad \text{(R4)}$$

where C_xN^* represents pyridinic/pyrrolic N groups. In addition, the oxygen functional groups with electron-acceptor properties, such as carbonyl and quinone groups, may also induce the redox reactions during the electron-transfer process, which is expressed as eq R5[42]

$$C_xO^* + H^+ + e^- \leftrightarrow C_xOH \quad \text{(R5)}$$

where C_xO^* represents carbonyl and quinone groups and e^- represents electrons.

The CV curves of CD@AC-12 in Figure 6c further prove the above speculation. When the CDs were added into ACs with the ratio of 1:2, the encircled rectangular area was a decreasing trend with the faradaic peak. This demonstrates that the capacitance, resulting from electric double-layer behavior and faradaic reaction, is significantly enhanced by the amount of CD addition. As a result, an appropriate amount of the CD additive plays a crucial role in enhancing the specific capacitance of SCs.

The GCD measurements were carried out in the potential window of 0−1 V and at a current density of 0.25 A g^{-1}. As shown in Figure 8a, it should be noticed that the charging and discharging times gradually increase with the amount of the CD addition. The specific capacitances calculated based on the GCD results at various current densities are shown in Figure 8b. The capacitance of the CD@AC-11 electrode reaches as high as 301.7 F g^{-1} at 0.15 A g^{-1}, which is 2-fold higher than that of the AC one (i.e., 125.8 F g^{-1}). This is consistent with previous CV measurements, revealing the effectiveness of CD addition on the enhanced capacitance. As the specific capacitance of CD@AC-12 achieves 191.8 F g^{-1}, there is *ca.*

https://dx.doi.org/10.1021/acsomega.1c00448
ACS Omega 2021, 6, 7851−7861

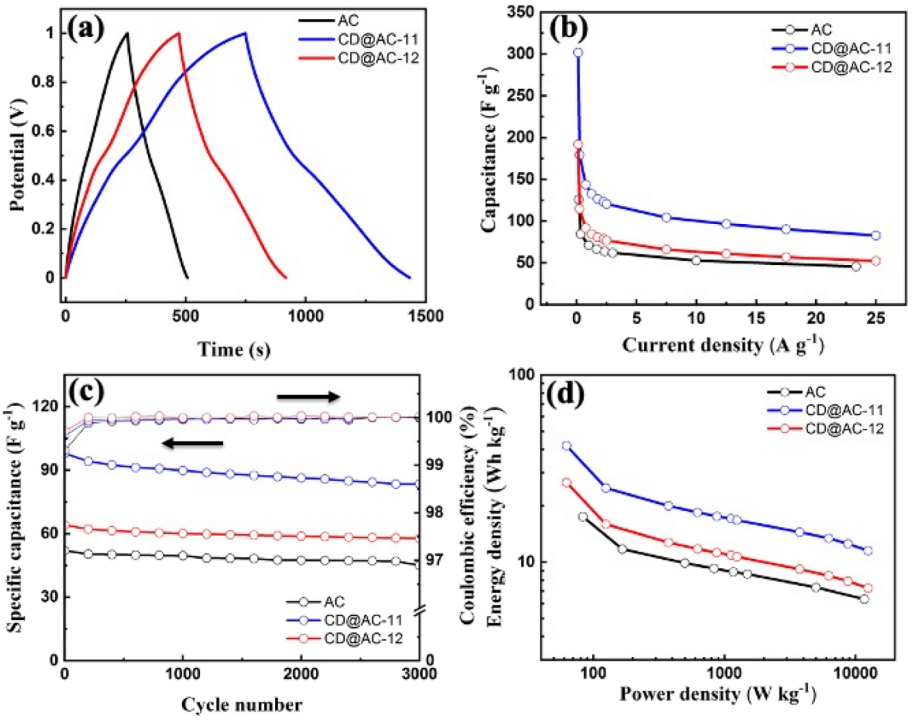

Figure 8. (a) GCD curves charged and discharged at 0.25 A g^{-1}, (b) variation of specific capacitance of electrodes with current densities, (c) cyclic performance of as-prepared electrodes at a current density of 15 A g^{-1} for 3000 cycles, and (d) Ragone plot of the SCs with as-prepared electrodes.

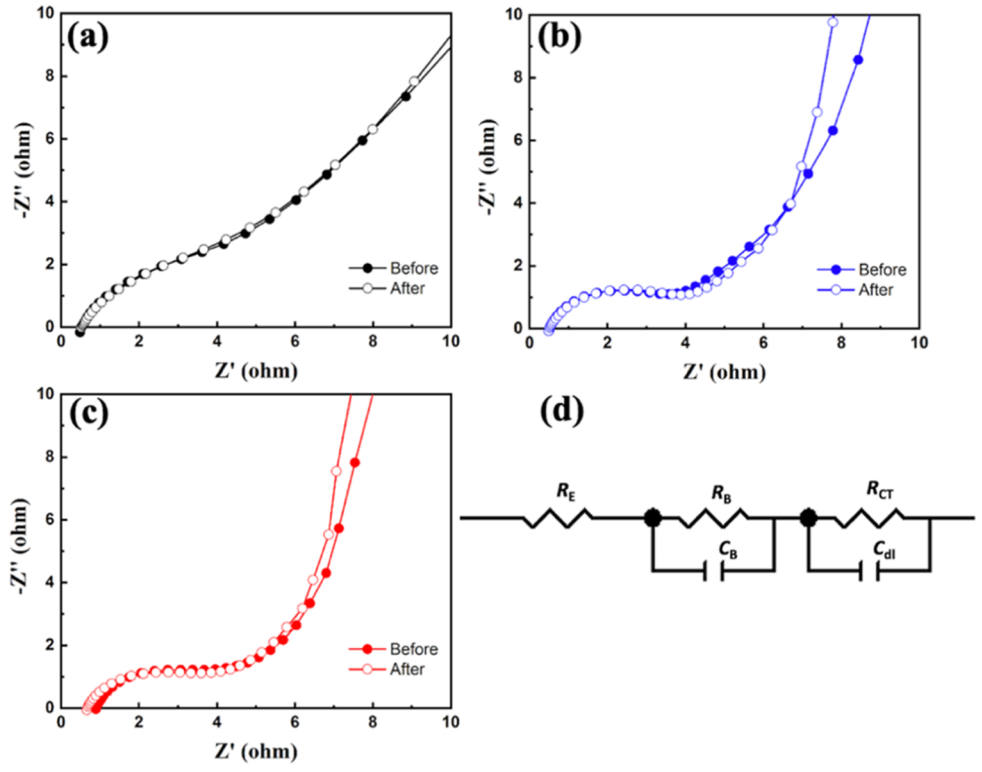

Figure 9. Nyquist plots of SCs fabricated with (a) AC, (b) CD@AC-11, and (c) CD@AC-12 electrodes and (d) proposed equivalent circuit for describing the impedance behavior.

52% increase achieved through adding half-amount CDs, confirming that the enhanced capacitance is proportional to the CD content in this range. Although the capacitance decreases with current density for all electrodes, the introduction of CDs still takes the effect as the doubled capacitance of AC even at high current densities, for example, 20 A g^{-1}.

The cyclic stability is also a key point to evaluate the performance of SCs. As shown in Figure 8c, the cyclic performance of as-prepared electrodes was analyzed at a

https://dx.doi.org/10.1021/acsomega.1c00448
ACS Omega 2021, 6, 7851−7861

current density of 15 A g^{-1}. After 3000 continuous cycles, all SC devices exhibit stable capacitance with an excellent coulombic efficiency (>99.5%). All SCs enable high capacitance retention with above 85% of the initial capacitance. Finally, the Ragone plots of the SCs with as-prepared electrodes are given in Figure 8d. The energy density and power density were calculated based on the following equations[47,48]

$$E = \frac{C(\Delta V)^2}{2} \quad \text{(R6)}$$

$$P = \frac{E}{\Delta t} \quad \text{(R7)}$$

where E is the specific energy density (W h kg^{-1}), C is the specific capacitance (F g^{-1}), ΔV (V) stands for the potential window, P is the specific power density (W kg^{-1}), and Δt (s) is the discharge time. The AC-based SC delivers an energy density of 18 W h kg^{-1} at a power density of 83 W kg^{-1}, and the energy density of 6 W h kg^{-1} can be delivered at 11,667 W kg^{-1}. In contrast, the energy density of the CD@AC-11 electrode can reach as high as 42 W h kg^{-1} at 63 W kg^{-1}, and even at a high power density of 12,500 W kg^{-1}, the energy density of 11 W h kg^{-1} can still be realized. At the same power density, the energy density of the CD@AC-11 electrode achieves double that of the AC one. Again, the addition of CD benefits the performance of SCs including the enhanced capacitance and superior cyclic stability. This result is superior to many of CD-based EDLC electrode materials (CDs/graphene,[49] GQDs/carbon fiber/graphene hydrogel,[50] GQDs/graphene oxide,[51] GQDs/ultramicroporous carbons,[38] etc.), as shown in Table S2 (see the Supporting Information).

To further check the ionic transportation and electronic conductivity of as-fabricated SCs, we applied the electrochemical impedance spectroscopy experiments before and after potential cycling (i.e., GCD 3000 cycles). The Nyquist plots of SCs in the frequency range of 100 kHz to 10 mHz are presented in Figure 9. Usually, the diameter of the semicircle in the high-frequency region can be inferred from the charge-transfer resistance. An equivalent circuit is proposed in Figure 9d to predict the impedance behavior from 100 kHz to 50 Hz. The equivalent circuit mainly contains the following elements: the resistance from the electrolyte solution (R_E), the interfacial resistance (R_B) and the capacitance (C_B) which results from the impedance between carbon electrodes and current collectors, the double-layer capacitance (C_{dl}), and the charge-transfer resistance (R_{CT}). The overall resistance, including R_E, R_B, and R_{CT}, represents the equivalent series resistance (R_{ES}).[19] The calculated results, analyzed by Z-view software, are shown in Table 1. We observe that the R_E only takes a very small contribution to the overall resistance and all R_E values are similar among the electrodes. The R_B values of CD@AC-11 and CD@AC-12 are slightly higher than that of the AC sample, indicating that the influence of the CD additive on the interfacial resistance is insignificant. However, the R_{CT}, which acts as a major contributor to R_{ES}, is apparently decreased after adding the CD additive into the AC electrode. The R_{ES} of CD@AC-11 is approximately 50% smaller than that of AC, indicating that the introduction of CDs strongly decreases the overall inner resistance of the AC-based electrode. The improved electrochemical impedance can be attributed to the fact that the higher surface coverage provided by the CDs facilitates a rapid double-layer formation and smooth charge transfer, thus decreasing the overall resistance. After cycling, the R_{ES} of the AC electrode maintains an identical value, while the R_{ES} values of CD@AC-11 and CD@AC-12 electrodes display a slight decrease, proving the presence of a robust carbon framework. Since there is no decay after thousands of cycling processes, this result confirms satisfactory cyclic stability of the devices.

Table 1. Calculated Equivalent Resistance Values in the High-Frequency Region and Diffusion Coefficients of H^+ Ions in SCs

electrode	R_E (Ω)	R_B (Ω)	R_{CT} (Ω)	R_{ES} (Ω)	D (cm^2 s^{-1})
			before cycling		
AC	0.50	1.11	8.16	9.77	1.34×10^{-12}
CD@AC-11	0.56	1.86	2.18	4.60	1.64×10^{-11}
CD@AC-12	0.52	2.09	2.59	5.66	1.21×10^{-11}
			after cycling		
AC	0.51	1.13	8.17	9.81	2.41×10^{-12}
CD@AC-11	0.55	1.19	2.45	4.19	1.05×10^{-10}
CD@AC-12	0.54	1.55	2.28	4.57	6.14×10^{-11}

In the low-frequency range, the slope of the linear line suggests that the electrochemical impedance was dominated by ionic diffusion. The larger of the slope, the lower of the resistance is achieved.[52] Accordingly, the ionic diffusion coefficient could be calculated based on the following equation[19,53]

$$k_w = \frac{RT}{n^2F^2A\sqrt{2}}\left(\frac{1}{D^{1/2}C^*}\right) \quad \text{(R8)}$$

where k_w can be obtained by the slope of the line and the D value reflects the diffusivity of H^+ ions in electrodes. All other parameters in this equation are known values, where n is the charge-transfer number, A is the electrode surface area, and C^* is the ionic concentration.[19] The calculated D values are also shown in Table 1. Before cycling, the ionic diffusion coefficient for CD@AC-11 shows 12.2 times higher than that of the pristine AC. The enhanced ionic diffusion coefficient is observed because the hydrophilic CDs make it easier for the ions and hydration molecules to access the interior carbon framework (i.e., a shorter diffusion path and higher hydrophilic surface coverage). After cycling, the ionic diffusion coefficient for the CD@AC-11 electrode is enhanced by 25.5 times as compared to that of the pristine AC one. This finding mainly originates from a synergistic effect that combines hydrophilic sites (from CDs) and lateral interactions with dipole moments of hydration molecules, leading to a higher wetted surface area by electrolyte wetting, that is, reaching a complete wetting after an appropriate period. In other words, after thousands of charging and discharging processes, the CD@AC-11 electrode is completely wetted, making high pore accessibility for ionic transportation. Accordingly, the improved D value of CD@AC-11 confirms that the existence of functionalized binding sites enables the creation of more accessible SSAs and shortens the ionic diffusion path.

On the basis of experimental results, the role of the CD additive in enhancing the specific capacitance of highly porous AC electrodes requires an in-depth investigation. First, the existence of the CDs imparts a surface polarity, which greatly improves the wettability of the internal nanostructures of porous carbon electrodes. As shown in Figure 10a, it is generally recognized that AC possesses a well-developed porous structure, consisting of mesopores (pore size: 2−50

https://dx.doi.org/10.1021/acsomega.1c00448
ACS Omega 2021, 6, 7851−7861

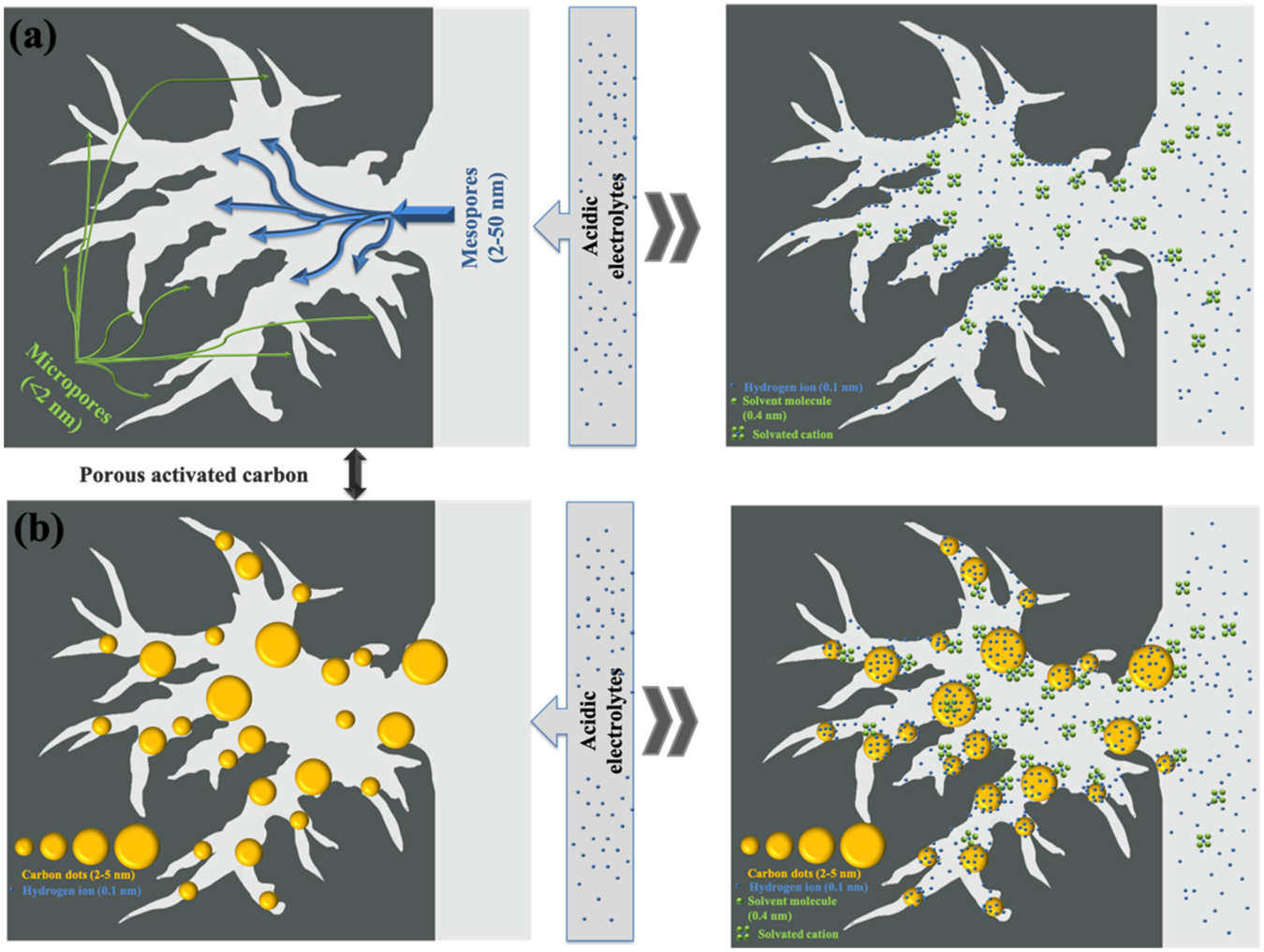

Figure 10. Schematic illustrations of the charging process in (a) AC and (b) CD@AC-11 electrodes.

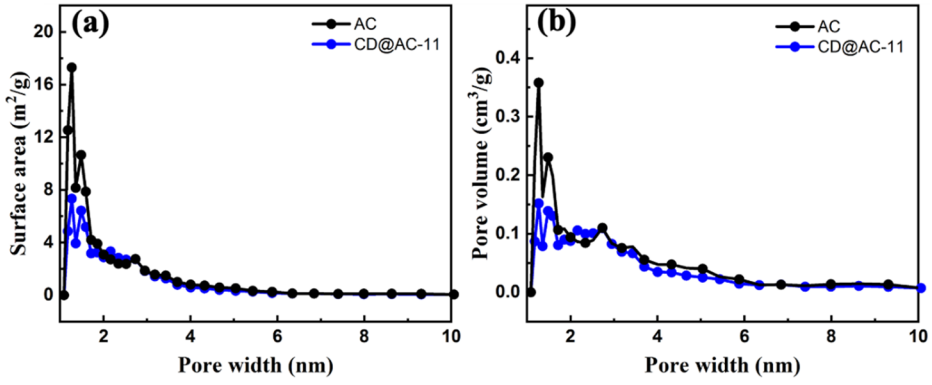

Figure 11. (a,b) DFT pore size distributions of AC and CD@AC-11 samples.

nm) and micropores (pore size: < 2 nm). Thus, the deep and branched micropores restrict the ion movement, resulting in a long ionic diffusion pathway during the charging process.[13] With the well-distributed CDs on the surface, more ions are favorably accessible to the inner pores, thus enhancing the wettability of the AC electrodes. Second, a large amount of hydrophilic polar sites exists, thus creating more accessible surface area. As shown in Figure 10b, with the aid of the robust and stable AC matrix, the nanosized CDs (average particle size: 2−5 nm) can be evenly deposited on the surface or into the porous structure, generating a large number of CD binding sites.

However, the CD deposits inside the pore channels possibly hinder ionic diffusion at the entrance of micropores, as illustrated in Figure 10b. Table S1 (see the Supporting Information) shows surface characteristics of the pristine and CD@AC-11 composites including the BET surface area, total pore volume, and pore size distribution, determined by nitrogen physisorption at −196 °C. We observe that pristine AC is mainly microporous, whereas the micropore fraction is

https://dx.doi.org/10.1021/acsomega.1c00448
ACS Omega 2021, 6, 7851−7861

decreased by the introduction of CDs. Figure 11a,b shows the DFT pore size distributions of different carbons, indicating that the pore size distribution could be controlled by the addition of CDs in the carbon composites. It is of interest that both the specific capacitance and diffusion coefficient are significantly enhanced by an increase in mesopore fraction of the carbon composites. This demonstrates that the above postulation (see Figure 10) is successfully established. This result reveals that the entrance of micropore channels is partly occupied by the CDs. Fortunately, the mesopore channel is still open accessible for ions or hydration molecules during the charge/discharge process. Meanwhile, the AC can be considered as a robust matrix that provides a well-developed porous framework bearing well-dispersed CDs. The CDs not only improve the ionic diffusion pathway but also offer a large number of hydrophilic sites (i.e., high surface coverage of the accessible surface area for electrolyte wetting), enabling the enhanced capacitance. Thus, this structural CD@AC design can be utilized for engineering the desired pore structure and micropore/mesopore fraction within the AC electrodes.

4. CONCLUSIONS

In summary, we achieved superior performance of SCs with the well-distributed CDs decorating the surface of the AC matrix. The introduction of hydrophilic CDs not only improved the wettability of electrodes but also created electroactive sites. The capacitance was greatly improved from 125.8 to 301.7 F g^{-1} due to the enlarged effective surface area and enhanced electrochemical activity without sacrificing the high cyclability. With the existence of abundant polar sites, ions are attracted to and accumulate around the CDs, therefore shortening ionic diffusion paths and decreasing the inner resistance. Our work indicates that the CDs could be well dispersed on the carbon matrix and the effective surface area could be significantly improved *via* creating numberless functionalized CD sites, resulting in the enhanced electric double-layer capacitance as well as pseudo-capacitance. The unique carbon composite can be utilized for engineering the desired pore structure and micropore/mesopore fraction within the AC electrodes. This design of a decorated carbon framework possesses great potential for developing promising energy-storage devices in the near future.

■ ASSOCIATED CONTENT

Supporting Information

The Supporting Information is available free of charge at https://pubs.acs.org/doi/10.1021/acsomega.1c00448.

BET surface area, total pore volume, and pore size distribution of AC and CD@AC-11 samples and summary of various C-QD-based EDLC electrode materials (PDF)

■ AUTHOR INFORMATION

Corresponding Authors

Chien-Te Hsieh − *Department of Chemical Engineering and Materials Science, Yuan Ze University, Taoyuan 32003, Taiwan; Department of Mechanical, Aerospace, and Biomedical Engineering, The University of Tennessee, Knoxville, Tennessee 37996, United States;* orcid.org/0000-0002-1053-8635; Email: cthsieh@saturn.yzu.edu.tw

David P. Harper − *Center for Renewable Carbon, Institute of Agriculture and Department of Materials Science and Engineering, The University of Tennessee, Knoxville, Tennessee 37996, United States;* orcid.org/0000-0003-2783-5406; Email: dharper4@utk.edu

Authors

Lu Yu − *Center for Renewable Carbon, Institute of Agriculture and Department of Materials Science and Engineering, The University of Tennessee, Knoxville, Tennessee 37996, United States*

David J. Keffer − *Department of Materials Science and Engineering, The University of Tennessee, Knoxville, Tennessee 37996, United States;* orcid.org/0000-0002-6246-0286

Hao Chen − *Department of Chemistry, The University of Tennessee, Knoxville, Tennessee 37996, United States;* orcid.org/0000-0002-6658-4198

Gabriel A. Goenaga − *Department of Chemical and Biomolecular, The University of Tennessee, Knoxville, Tennessee 37996, United States*

Sheng Dai − *Department of Chemistry, The University of Tennessee, Knoxville, Tennessee 37996, United States; Chemical Sciences Division, Oak Ridge National Laboratory, Oak Ridge, Tennessee 37831, United States;* orcid.org/0000-0002-8046-3931

Thomas A. Zawodzinski − *Department of Chemical and Biomolecular, The University of Tennessee, Knoxville, Tennessee 37996, United States; Physical Chem. Mater. Group, Oak Ridge National Laboratory, Oak Ridge, Tennessee 37831, United States;* orcid.org/0000-0002-2690-8784

Complete contact information is available at: https://pubs.acs.org/10.1021/acsomega.1c00448

Notes

The authors declare no competing financial interest.

■ ACKNOWLEDGMENTS

The authors would like to thank Dr. John Dunlap and Dr. Gerd Duscher (Joint Institute for Advanced Materials) for their help and support for conducting the TEM measurements. The authors would also like to thank Kendhl Seabright (CRC UT-Knoxville) for conducting the CHNS measurements. The authors would also like to thank Dr. Tao Wu and Dr. Teng Li (Food science, UTIA) for their support for contact angle measurements. This research was supported by a grant from the U.S. Department of Energy BioEnergy Technologies Office through the Biomass Research and Development Initiative award DE-EE0008353.0000. D.P.H. acknowledges support from the USDA National Institute of Food and Agriculture Hatch Project 1012359.

■ REFERENCES

(1) Zhu, Y.; Murali, S.; Stoller, M. D.; Ganesh, K. J.; Cai, W.; Ferreira, P. J.; Pirkle, A.; Wallace, R. M.; Cychosz, K. A.; Thommes, M.; Su, D.; Stach, E. A.; Ruoff, R. S. Carbon-based supercapacitors produced by activation of graphene. *Science* **2011**, *332*, 1537−1541.

(2) Vlad, A.; Balducci, A. Porous materials get energized. *Nat. Mater.* **2017**, *16*, 161−162.

(3) Forse, A. C.; Merlet, C.; Griffin, J. M.; Grey, C. P. New Perspectives on the Charging Mechanisms of Supercapacitors. *J. Am. Chem. Soc.* **2016**, *138*, 5731−5744.

(4) Guan, B. Y.; Yu, L.; Wang, X.; Song, S.; Lou, X. W. Formation of Onion-Like NiCo2 S4 Particles via Sequential Ion-Exchange for Hybrid Supercapacitors. *Adv. Mater.* **2017**, *29*, 1605051.

(5) Qing, Y.; Jiang, Y.; Lin, H.; Wang, L.; Liu, A.; Cao, Y.; Sheng, R.; Guo, Y.; Fan, C.; Zhang, S.; Jia, D.; Fan, Z. Boosting the supercapacitor performance of activated carbon by constructing overall conductive networks using graphene quantum dots. *J. Mater. Chem. A* **2019**, *7*, 6021−6027.
(6) Wang, G.; Zhang, L.; Zhang, J. A review of electrode materials for electrochemical supercapacitors. *Chem. Soc. Rev.* **2012**, *41*, 797−828.
(7) Najib, S.; Erdem, E. Current progress achieved in novel materials for supercapacitor electrodes: mini review. *Nanoscale Adv.* **2019**, *1*, 2817−2827.
(8) Salanne, M.; Rotenberg, B.; Naoi, K.; Kaneko, K.; Taberna, P. L.; Grey, C. P.; Dunn, B.; Simon, P. Efficient storage mechanisms for building better supercapacitors. *Nat. Energy* **2016**, *1*, 16070.
(9) Simon, P.; Gogotsi, Y. Materials for electrochemical capacitors. *Nat. Mater.* **2008**, *7*, 845−854.
(10) Lyu, L.; Seong, K.-d.; Ko, D.; Choi, J.; Lee, C.; Hwang, T.; Cho, Y.; Jin, X.; Zhang, W.; Pang, H.; Piao, Y. Recent development of biomass-derived carbons and composites as electrode materials for supercapacitors. *Mater. Chem. Front.* **2019**, *3*, 2543−2570.
(11) Béguin, F.; Presser, V.; Balducci, A.; Frackowiak, E. Carbons and electrolytes for advanced supercapacitors. *Adv. Mater.* **2014**, *26*, 2219−2251.
(12) Hulicova-Jurcakova, D.; Puziy, A. M.; Olga, I. P.; Fabian, S.-G.; Tascon, J. M. D.; Liu, G. Q. Highly Stable Performance of Supercapacitors from Phosphorus-Enriched Carbons. *J. Am. Chem. Soc.* **2009**, *131*, 5026−5027.
(13) Pandolfo, A. G.; Hollenkamp, A. F. Carbon properties and their role in supercapacitors. *J. Power Sources* **2006**, *157*, 11−27.
(14) Deng, Y.; Xie, Y.; Zou, K.; Ji, X. Review on recent advances in nitrogen-doped carbons: preparations and applications in supercapacitors. *J. Mater. Chem. A* **2016**, *4*, 1144−1173.
(15) Chen, X.; Zhang, J.; Zhang, B.; Dong, S.; Guo, X.; Mu, X.; Fei, B. A novel hierarchical porous nitrogen-doped carbon derived from bamboo shoot for high performance supercapacitor. *Sci. Rep.* **2017**, *7*, 7362.
(16) Zhou, X.; Wang, P.; Zhang, Y.; Wang, L.; Zhang, L.; Zhang, L.; Xu, L.; Liu, L. Biomass based nitrogen-doped structure-tunable versatile porous carbon materials. *J. Mater. Chem. A* **2017**, *5*, 12958−12968.
(17) Liu, M.; Niu, J.; Zhang, Z.; Dou, M.; Wang, F. Potassium compound-assistant synthesis of multi-heteroatom doped ultrathin porous carbon nanosheets for high performance supercapacitors. *Nano Energy* **2018**, *51*, 366−372.
(18) Zhang, Y.; Liu, S.; Zheng, X.; Wang, X.; Xu, Y.; Tang, H.; Kang, F.; Yang, Q.-H.; Luo, J. Biomass Organs Control the Porosity of Their Pyrolyzed Carbon. *Adv. Funct. Mater.* **2017**, *27*, 1604687.
(19) Hsieh, C.-T.; Hsu, S.-M.; Lin, J.-Y.; Teng, H. Electrochemical Capacitors Based on Graphene Oxide Sheets Using Different Aqueous Electrolytes. *J. Phys. Chem. C* **2011**, *115*, 12367−12374.
(20) Fan, Z.; Yan, J.; Wei, T.; Zhi, L.; Ning, G.; Li, T.; Wei, F. Asymmetric Supercapacitors Based on Graphene/MnO2 and Activated Carbon Nanofiber Electrodes with High Power and Energy Density. *Adv. Funct. Mater.* **2011**, *21*, 2366−2375.
(21) Wei, J.-S.; Ding, H.; Zhang, P.; Song, Y.-F.; Chen, J.; Wang, Y.-G.; Xiong, H.-M. Carbon Dots/NiCo2O4Nanocomposites with Various Morphologies for High Performance Supercapacitors. *Small* **2016**, *12*, 5927−5934.
(22) García-Negrón, V.; Phillip, N. D.; Li, J.; Daniel, C.; Wood, D.; Keffer, D. J.; Rios, O.; Harper, D. P. Processing-Structure-Property Relationships for Lignin-Based Carbonaceous Materials Used in Energy-Storage Applications. *Energy Technol.* **2017**, *5*, 1311−1321.
(23) Fu, K.; Yue, Q.; Gao, B.; Sun, Y.; Zhu, L. Preparation, characterization and application of lignin-based activated carbon from black liquor lignin by steam activation. *Chem. Eng. J.* **2013**, *228*, 1074−1082.
(24) Gonzalez-Serrano, E.; Cordero, T.; Rodríguez-Mirasol, J.; Rodríguez, J. J. Development of Porosity upon Chemical Activation of Kraft Lignin with ZnCl2. *Ind. Eng. Chem. Res.* **1997**, *36*, 4832−4838.
(25) Maldhure, A. V.; Ekhe, J. D. Preparation and characterizations of microwave assisted activated carbons from industrial waste lignin for Cu(II) sorption. *Chem. Eng. J.* **2011**, *168*, 1103−1111.
(26) Hayashi, J.; Kazehaya, A.; Muroyama, K.; Watkinson, A. P. Preparation of activated carbon from lignin by chemical activation. *Carbon* **2000**, *38*, 1873−1878.
(27) Gu, S.; Hsieh, C.-T.; Ashraf Gandomi, Y.; Chang, J.-K.; Li, J.; Li, J.; Zhang, H.; Guo, Q.; Lau, K. C.; Pandey, R. Microwave growth and tunable photoluminescence of nitrogen-doped graphene and carbon nitride quantum dots. *J. Mater. Chem. C* **2019**, *7*, 5468−5476.
(28) Gu, S.; Hsieh, C.-T.; Ashraf Gandomi, Y.; Li, J.; Yue, X. X.; Chang, J.-K. Tailoring fluorescence emissions, quantum yields, and white light emitting from nitrogen-doped graphene and carbon nitride quantum dots. *Nanoscale* **2019**, *11*, 16553−16561.
(29) Hu, C.; Li, M.; Qiu, J.; Sun, Y.-P. Design and fabrication of carbon dots for energy conversion and storage. *Chem. Soc. Rev.* **2019**, *48*, 2315−2337.
(30) Liu, W.-W.; Feng, Y.-Q.; Yan, X.-B.; Chen, J.-T.; Xue, Q.-J. Superior Micro-Supercapacitors Based on Graphene Quantum Dots. *Adv. Funct. Mater.* **2013**, *23*, 4111−4122.
(31) Zhang, Z.; Zhang, J.; Chen, N.; Qu, L. Graphene quantum dots: an emerging material for energy-related applications and beyond. *Energy Environ. Sci.* **2012**, 8869.
(32) Yang, X.; Hu, D.; Zhang, P.; Ding, H.; Ji, Y.; Zou, H.; Li, B.; Wei, J.; Wei, X. Integrated Carbon Dots-Matrix Structures: An Efficient Strategy for High-Performance Electric Double Layer Capacitors. *ACS Appl. Energy Mater.* **2020**, *3*, 4958−4964.
(33) Wei, J.-S.; Song, T.-B.; Zhang, P.; Zhu, Z.-Y.; Dong, X.-Y.; Niu, X.-Q.; Xiong, H.-M. Integrating Carbon Dots with Porous Hydrogels to Produce Full Carbon Electrodes for Electric Double-Layer Capacitors. *ACS Appl. Energy Mater.* **2020**, *3*, 6907−6914.
(34) Hou, H.; Banks, C. E.; Jing, M.; Zhang, Y.; Ji, X. Carbon Quantum Dots and Their Derivative 3D Porous Carbon Frameworks for Sodium-Ion Batteries with Ultralong Cycle Life. *Adv. Mater.* **2015**, *27*, 7861−7866.
(35) Xiong, T.; Cen, W.; Zhang, Y.; Dong, F. Bridging the g-C3N4 Interlayers for Enhanced Photocatalysis. *ACS Catal.* **2016**, *6*, 2462−2472.
(36) Niu, S.; McFeron, R.; Godínez-Salomón, F.; Chapman, B. S.; Damin, C. A.; Tracy, J. B.; Augustyn, V.; Rhodes, C. P. Enhanced Electrochemical Lithium-Ion Charge Storage of Iron Oxide Nanosheets. *Chem. Mater.* **2017**, *29*, 7794−7807.
(37) Pelka, R.; Pattek-Janczyk, A.; Arabczyk, W. Studies of the Oxidation of Nanocrystalline Iron with Oxygen by means of TG, MS, and XRD Methods. *J. Phys. Chem. C* **2008**, *112*, 13992−13996.
(38) Zhang, S.; Zhu, J.; Qing, Y.; Wang, L.; Zhao, J.; Li, J.; Tian, W.; Jia, D.; Fan, Z. Ultramicroporous Carbons Puzzled by Graphene Quantum Dots: Integrated High Gravimetric, Volumetric, and Areal Capacitances for Supercapacitors. *Adv. Funct. Mater.* **2018**, *28*, 1805898.
(39) Jian, X.; Li, J.-g.; Yang, H.-m.; Cao, L.-l.; Zhang, E.-h.; Liang, Z.-h. Carbon quantum dots reinforced polypyrrole nanowire via electrostatic self-assembly strategy for high-performance supercapacitors. *Carbon* **2017**, *114*, 533−543.
(40) Hoang, V. C.; Nguyen, L. H.; Gomes, V. G. High efficiency supercapacitor derived from biomass based carbon dots and reduced graphene oxide composite. *J. Electroanal. Chem.* **2019**, *832*, 87−96.
(41) Li, B.; Dai, F.; Xiao, Q.; Yang, L.; Shen, J.; Zhang, C.; Cai, M. Nitrogen-doped activated carbon for a high energy hybrid supercapacitor. *Energy Environ. Sci.* **2016**, *9*, 102−106.
(42) Hsieh, C.-T.; Teng, H. Influence of oxygen treatment on electric double-layer capacitance of activated carbon fabrics. *Carbon* **2002**, *40*, 667−674.
(43) Zheng, J. P.; Huang, J.; Jow, T. R. The Limitations of Energy Density for Electrochemical Capacitors. *J. Electrochem. Soc.* **1997**, *144*, 2026−2031.
(44) Lota, G.; Grzyb, B.; Machnikowska, H.; Machnikowski, J.; Frackowiak, E. Effect of nitrogen in carbon electrode on the supercapacitor performance. *Chem. Phys. Lett.* **2005**, *404*, 53−58.

https://dx.doi.org/10.1021/acsomega.1c00448
ACS Omega 2021, 6, 7851−7861

(45) Lota, G.; Lota, K.; Frackowiak, E. Nanotubes based composites rich in nitrogen for supercapacitor application. *Electrochem. Commun.* **2007**, *9*, 1828−1832.
(46) Khattak, A. M.; Ghazi, Z. A.; Liang, B.; Khan, N. A.; Iqbal, A.; Li, L.; Tang, Z. A redox-active 2D covalent organic framework with pyridine moieties capable of faradaic energy storage. *J. Mater. Chem. A* **2016**, *4*, 16312−16317.
(47) Zhou, L.; Cao, H.; Zhu, S.; Hou, L.; Yuan, C. Hierarchical micro-/mesoporous N- and O-enriched carbon derived from disposable cashmere: a competitive cost-effective material for high-performance electrochemical capacitors. *Green Chem.* **2015**, *17*, 2373−2382.
(48) Zhang, J.; Chen, Z.; Wang, G.; Hou, L.; Yuan, C. Eco-friendly and scalable synthesis of micro-/mesoporous carbon sub-microspheres as competitive electrodes for supercapacitors and sodium-ion batteries. *Appl. Surf. Sci.* **2020**, *533*, 147511.
(49) Li, Q.; Cheng, H.; Wu, X.; Wang, C.-F.; Wu, G.; Chen, S. Enriched carbon dots/graphene microfibers towards high-performance micro-supercapacitors. *J. Mater. Chem. A* **2018**, *6*, 14112−14119.
(50) Li, Z.; Wei, J.; Ren, J.; Wu, X.; Wang, L.; Pan, D.; Wu, M. Hierarchical construction of high-performance all-carbon flexible fiber supercapacitors with graphene hydrogel and nitrogen-doped graphene quantum dots. *Carbon* **2019**, *154*, 410−419.
(51) Luo, P.; Guan, X.; Yu, Y.; Li, X.; Yan, F. Hydrothermal Synthesis of Graphene Quantum Dots Supported on Three-Dimensional Graphene for Supercapacitors. *Nanomaterials* **2019**, *9*, 201.
(52) Liang, H.; Lin, J.; Jia, H.; Chen, S.; Qi, J.; Cao, J.; Lin, T.; Fei, W.; Feng, J. Hierarchical NiCo-LDH/NiCoP@NiMn-LDH hybrid electrodes on carbon cloth for excellent supercapacitors. *J. Mater. Chem. A* **2018**, *6*, 15040−15046.
(53) Shi, M.; Chen, Z.; Sun, J. Determination of chloride diffusivity in concrete by AC impedance spectroscopy. *Cem. Concr. Compos.* **1999**, *29*, 1111.

https://dx.doi.org/10.1021/acsomega.1c00448
ACS Omega 2021, 6, 7851−7861